Bulk modulus of H_2O across the ice VII – ice X transition measured by time-resolved X-ray diffraction in dynamic Diamond Anvil Cell experiments

A. S. J. Méndez[1, 2], F. Trybel[2], R. J. Husband[1], G. Steinle-Neumann[2], H.-P. Liermann[1] and H. Marquardt[3]

[1]*Deutsches Elektronen-Synchrotron (DESY), 22607 Hamburg, Germany;* [2]*Bayerisches Geoinstitut, Universität Bayreuth, 95440 Bayreuth, Germany;* [3]*Department of Earth Sciences, University of Oxford, OX1 3AN Oxford, UK.*

*Corresponding author: Alba San José Méndez (alba.mendez@desy.de)

Abstract

We have studied the H_2O ice VII – ice X phase transition at room temperature by performing three quasi-continuous synchrotron time-resolved X-ray diffraction experiments in the dynamic Diamond Anvil Cell, reaching pressures of 180 GPa. The dense pressure-coverage of our volume data allows us to directly derive the bulk modulus for H_2O over the entire pressure range. Our data document three major changes in compression behavior in the ranges of 35-40, 50-55 and 90-110 GPa, likely corresponding to the formation of pre-transition dynamically disordered ice VII and ice X, and static ice X, respectively. Our results confirm that ice X has a very high bulk modulus.

1. INTRODUCTION

H_2O ice is present in a large variety of planetary bodies, including the ice giants, Uranus and Neptune, mini-Neptune exoplanets [1,2] and icy satellites [3,4], having a fundamental impact on the heat and chemical exchange in their interiors [5–8]. H_2O ice might also be present in Earth's deep mantle, as well as other terrestrial planets, where it can form through mineral dehydration reactions occuring at relatively cold regions of the mantle [9–11]. The polymorphs ice VII and ice X are the stable forms of H_2O ice that exist at pressures (P) larger

than 2 GPa, and their physical properties play a pivotal role in the structure and evolution of H_2O-rich planetary bodies.

Ice VII is a solid characterized by a body centered cubic (*bcc*) arrangement of oxygens, with H_2O molecules linked via hydrogen bonds (O-H···O) such that the ice-rules are satisfied [12]. The high-*P* phase ice X is based on the same *bcc* oxygen lattice, but hydrogen atoms are located symmetrically between two oxygen atoms (O-H-O). It has been proposed that the ice VII - ice X transition proceeds through a proton order-disorder transition through which H_2O molecules dissociate, triggered by changes in the energy potential for the O-H···O bond with *P*, leading to the formation of pre-transitional states prior to complete bond symmetrization in ice X [13–16]. At low *P*, the energy potential determining the position of the protons has been predicted to be of double-well character with a high energy barrier and a localized proton position coinciding with one of the two minima [17]. Computational studies [13–17] describe three main changes in the energy potential of the H-bond across the ice VII - ice X transition: (i) A lowering of the energy barrier with *P* triggers proton tunneling between the two minima, forming the translationally or dynamically disordered ice VII (ice VII'). (ii) As the potential barrier approaches zero with *P*, the proton distribution shifts to the center, forming the dynamically disordered ice X (ice X'). (iii) Symmetrization is complete when the energy potential adopts a narrow single-well form, localized at the mid-point between two oxygens (O-H-O), forming static ice X.

Numerous experimental studies employing different techniques, including X-ray [18,19] (XRD) and neutron diffraction [20], Raman [21] and infrared (IR) spectroscopy [22–25] as well as refractive index measurements [26], reported anomalies between 40 and 75 GPa, possibly associated with the formation of the dynamically disordered states. Diffraction [18,20,27] and IR-measurements [23,25] have reported O-H-O bond symmetrization in the *P*-range of 110-140 GPa, while Raman [28] and optical

measurements [26] suggest an onset at $P \approx$ 90 GPa. However, these experimental techniques do not probe proton dynamics directly, and the formation of the pre-transitional states cannot be detected unambiguously. Recently, Meier *et al*. [29] reported first direct observations of proton mobility for P=8-90 GPa by a line-shape analysis of Nuclear Magnetic Resonance (NMR) experiments.

Here we perform dynamic compression experiments in combination with time-resolved XRD in order to explore the compressive behavior of H_2O across the ice VII – ice X transition up to 180 GPa using a dynamic Diamond Anvil Cell (dDAC) driven by a piezoelectric actuator [30,31]. This setup provides quasi-continuous volume-P data, with hundreds of diffraction patterns recorded in one experiment, and therefore allows us to compute compressibility by numerical differentiation without invoking an equation-of-state model to fit the data, a significant advance relative to prior static experiments with tens of data points. We track the bulk modulus evolution across the ice VII – ice X transition, and explore whether this transition as well as the pre-transitional states (ice VII' and ice X') can be detected from changes in the compression behavior.

2. METHODS

2.1. Experimental setup

Three symmetric piston cylinder-type DACs are equipped with 150, 100 and 80 µm diameter culet anvils (dDAC-1, dDAC-2 and dDAC-3), with two different gasket configurations (Table 1): (i) In dDAC-2 and dDAC-3, regular Re gaskets are pre-indented to a thickness of 30 µm and holes of 50 and 40 µm diameters are drilled, respectively; (ii) In dDAC-1, an amorphous gasket is employed in order to avoid the emergence of strong diffraction peaks from the Re gasket that may overwhelm the diffraction patterns of H_2O with smaller scattering factors. A disk of an amorphous boron alloy ($Fe_{0.79}Si_{0.06}B_{0.15}$) with a thickness of 30 µm and a 50 µm

diameter hole is inserted in a Re gasket, pre-indented to the same thickness, following the procedure described in Méndez *et al.* [32].

Milli-Q H_2O is loaded along with Au powder (99.99% pure from Sigma Aldrich) as *P*-marker and a ruby chip to monitor *P* in the sample during pre-compression. DACs are inserted in a "cap housing" coupled to a high-voltage piezoelectric actuator (PEA) as described in Jenei *et al.* [31] DAC and PEA are coupled by tightening the end cap at the back of the housing until a *P*-increase of 1-2 GPa is observed. The PEA is connected to an amplifier (Piezosystem Jena GmbH), remotely controlled via a waveform generator (Agilent 33522B). When voltage is applied, the PEA in contact with the DAC expands, pushing directly onto the piston and compressing the sample. Trapezoidal voltage-time waveforms are created by the Agilent Benchlink waveform builder software by Keysight and sent to the PEA. We apply voltage-time waveforms with a constant compression rate in each experiment, corresponding to nominal *P*-rates of 0.4-0.6 GPa/s that permits for sufficiently long X-ray exposure times while still achieving an excellent resolution in *P*-sampling (Table 1).

Table 1. Summary of experimental run conditions

Run #	Culet size (µm)	Gasket type	Sample-detector distance (mm)	Maximum pressure (GPa)	Experiment total time (s)	Nominal compression rate (GPa/s)	Exposure time (ms)	Number of images analyzed
dDAC-1	150	Amorphous	418.42	90	300	0.5	100	1800
dDAC-2	100	Re	166.31	160	850	0.4	1000	590
dDAC-3	80	Re	404.89	180	868	0.6	2000	305

2.2. X-ray diffraction

Monochromatic synchrotron X-rays with a fixed wavelength (0.4828 Å) are used for time-resolved diffraction experiments at the Extreme Conditions Beamline P02.2 at PETRA III, Hamburg, Germany [33]. A compound refractive lens-focused X-ray beam (3 µm (h) x 8 µm

(v) FWHM) is aligned with the center of the sample chamber. GaAs 2.3 MPix LAMBDA detectors, with a pixel size of 55 µm x 55 µm and a repetition rate of up to 2 kHz, are employed to perform fast collection of XRD images [34,35]. For dDAC-2, one detector is aligned with the sample center and placed at a short sample-to-detector distance (Table 1), ensuring the collection of full diffraction rings. For dDAC-1 and dDAC-3, two detectorsare symmetrically offset from the direct beam, capturing sections of the Debye–Scherrer diffraction rings. Tilting of the detector(s) and the sample-detector distance are calibrated using a Cr_2O_3 standard (NIST 674b). With this setup we are able to collect more than 300 individual X-ray diffraction pattern in each compression experiment (Table 1). In-house data analysis software is used for quick visualization of the collected data (Fig. 1).

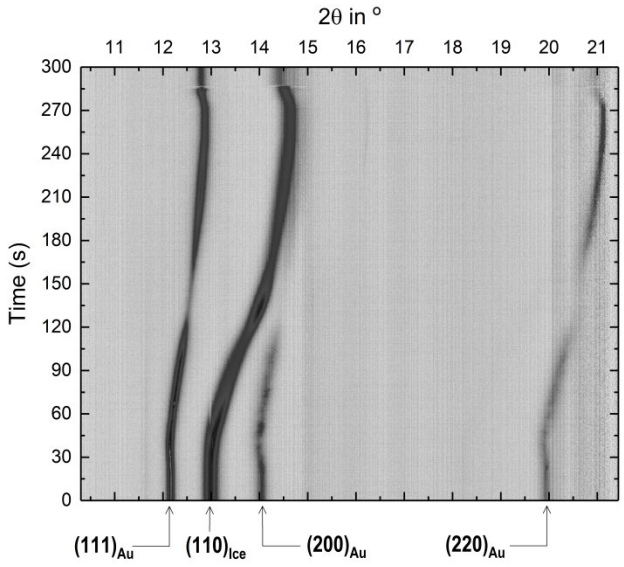

Figure 1. Contour plot showing the time-evolution of diffraction patterns (peaks) collected for dDAC-1 in time-2θ space; In our experiments, the (110) diffraction line of ice VII is the most intense and can be traced over the full *P*-range of the individual experiments.

2.3. Diffraction pattern fitting

The detector images are radially integrated using the Dioptas software [36] to obtain 1D diffraction patterns as a function of the 2θ-angle (Fig. 2). During integration, the dead areas of

111 the detectors are masked to improve the signal/noise ratio. Additionally, the most intense
112 areas of the (101) diffraction ring of Re – $(101)_{Re}$ – are masked in dDAC-2 in order to
113 minimize the convolution with the $(110)_{iceVII}$ diffraction ring (Fig. 3).

114

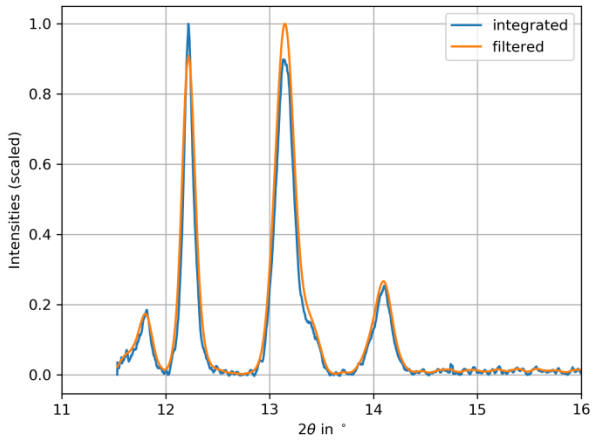

115

116 **Figure 2.** Exemplary integrated diffraction pattern for the dDAC-2 experiment at 26 GPa.
117 Blue shows the original pattern after integration of the detector image with Dioptas; orange
118 the pattern after application of an IIR filter with zero phase shift.

119 A python routine is developed to deal with the large number of diffraction patterns (Table 1)
120 and to automate peak fitting and tracking. Before integrated patterns are processed by the
121 routine, we average over three points in 2θ-space and apply an infinite impulse response (IIR)
122 filter forwards and backwards with zero phase shift to further improve the signal/noise ratio
123 and the reliability as well as the speed of the fitting routine (Fig. 2). In order to analyze the
124 recorded diffraction data, the peaks in the window 2θ=11.0°-20.0° are assigned to a crystal
125 structure, fitted and positions are tracked over the entire compression range in all diffraction
126 patterns. In a first step, the positions of the expected peaks (indices identified via peak
127 comparison with Dioptas) are calculated from the space group and a given initial compression
128 using a routine from the *pymatgen* (Python Materials Genomics) library [37]. The calculated
129 peak positions (*CPP*) are used as the initial positions for a model consisting of a Gaussian for

each peak and a linear background correction. The model is optimized with a non-linear least-squares fit to obtain optimal peak positions (*OPP*) employing the *LMFIT* package [38]. The *OPP* of the individual Gaussians are subsequently compared with the prediction (*CPP*); if an individual *OPP* is at larger (smaller) 2θ-angle than *CPP*, compression is increased (decreased) until $|OPP\text{-}CPP| < \epsilon$ is reached (with ϵ a convergence parameter). The optimization of the compression is performed with an adaptive step width to improve accuracy and runtime.

As the *P*-standard and the sample differ in compressional behavior, the peak positions are optimized separately: *P* is calculated using the optimized position of $(111)_{Au}$ combined with the equation-of-state of Fei *et al.* [39]. Volume (*V*) of H_2O ice is determined from $(110)_{iceVII}$. The $(200)_{Au}$ peak of the *P*-standard and $(101)_{Re}$ from the gasket (dDAC-2 and dDAC-3) are included to improve the model, but not considered in the optimization. In particular, $(200)_{Au}$ is not suitable for that purpose as (i) it is small in amplitude, (ii) the amplitude decreases with *P* and (iii) it starts to overlap with the $(110)_{iceVII}$ peak for *P*>50 GPa.

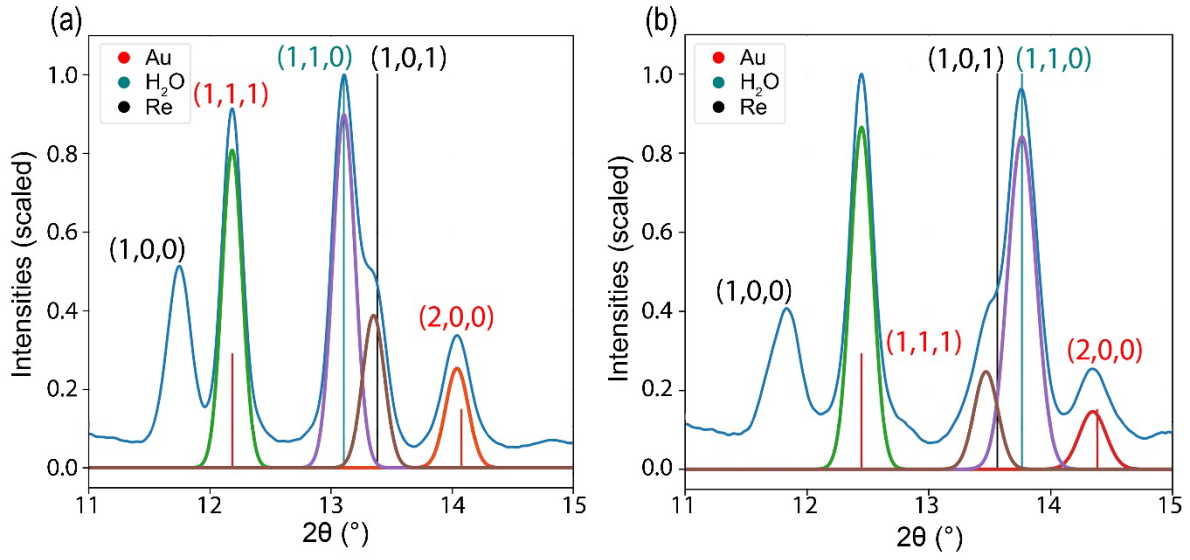

Figure 3. Diffraction patterns collected from dDAC-2 after application of the IRR filter (blue) at (a) 24 GPa and (b) 45 GPa with assigned indices and the calculated/theoretical peak positions (*CPP*) shown as vertical lines. The solid curves represent the Gaussian model peaks.

Diffraction patterns are individually loaded with user input on the initial compression estimate. Although the program can handle each spectrum individually, it is significantly more efficient to guess a starting compression from the previous *P*-step. This especially helps to resolve overlapping peaks, where a good initial guess is crucial. Such an interaction between $(110)_{IceVII}$ and $(101)_{Re}$ is shown in Fig. 3. At low *P*, $(110)_{IceVII}$ appears at a smaller 2θ-value than $(101)_{Re}$; during compression, the peaks start to overlap at $P > 20$ GPa and reverse order in 2θ at $P > 40$ GPa.

The routine can resolve the individual peaks while they are partly overlapping by estimating a linear compression rate. However, if the peaks are completely overlapping, a reliable fit is not possible, and, for this reason, for dDAC-3 a small *P*-range (41-49 GPa) is not processed. Nevertheless, we obtain, especially for dDAC-2 with a full diffraction ring, dense $V(P)$ data with only very small data scatter introduced by the fitting routine due to peak asymmetry and overlap. The error in *V* is calculated from the minimal separable peak distance in the routine (0.05° in 2θ). If the peak shift between two consecutive patterns is too small, the program tends to keep the positions constant, followed by a sudden jump to another configuration. In principle, this problem can be avoided by decreasing ϵ from 10^{-3} to 10^{-5} for $|OPP\text{-}CPP|$-determination. However, prohibitively increased computational requirements make fitting all patterns with $\epsilon=10^{-5}$ impossible. Instead, we use every 25th diffraction pattern for dDAC-1, every 10th for dDAC-2 and every 5th for dDAC-3, preserving an excellent *P*-resolution, i.e., 1 GPa for dDAC-1 and 3 GPa for dDAC-2 and dDAC-3.

Fitting a series of Gaussians rather than performing a Rietveld or Le Bail refinement has large advantages for the current datasets: (i) The standard refinement techniques rely on the peak shape which may cause problems for the peak-overlap discussed above and (ii) processing the data is even more challenging in terms of automation. Nevertheless, on a limited number of

diffraction patterns from dDAC-1 and dDAC-2 we have tested that P and V obtained from the Gaussian fitting performed here and a Le Bail refinement. The results are consistent with one another within the error coming from the minimal separable peak distance in our approach (Table 1 in the Supplemental Material).

2.4. Bulk modulus calculation

The isothermal bulk modulus (K_T) can be directly calculated from our dense $V(P)$ dataset via $K_T = -V \cdot \partial P/\partial V$, with the advantage that no assumption has to be made with respect to the analytical form of an equation-of-state. Previous DAC studies on ice VII and ice X [18,19,27], by contrast, had to rely on an equation-of-state fit due to the significantly lower number of data points. Here, using the increased P-spacing by not fitting all diffraction patterns as discussed above, becomes a further advantage, as a small denominator (ΔV) can lead to significant fluctuations in the calculated bulk modulus. We further apply spline interpolation with smoothing [40,41] before calculating the bulk modulus to mediate still existing unphysical fluctuations (Fig. S1 in the Supplemental Material) via a central difference scheme. The smoothing factors are chosen such that smooth variations of K_T with P are obtained, while simultaneously keeping the difference between data points and the spline <1% over the complete compression-range for all experiments (Fig. 4b).

The error in K_T is propagated from the error in V with a central difference scheme. As the $(111)_{Au}$ reflection (P-marker) does not suffer asymmetry or overlap, P is assumed to be error-free.

3. RESULTS AND DISCUSSION

3.1. Volume compression curve of H_2O ice

Figure 4 shows the unit cell V of H_2O ice as a function of P from our experiments in comparison with previous XRD measurements [18,19,27] and equation-of-state predictions [42,43]. Differences between V measured in our three runs fall within the refinement uncertainties determined by the resolution limit of 0.05° in 2θ for the diffraction patterns (Fig. 4a), suggesting that the choice of the gasket material or the sample-detector configuration do not affect the results significantly. Overall, our $V(P)$ data are in good agreement with previous experimental results [18,19,27] (Fig. 4c), and the observed differences in V between our three compression runs (dDAC-1, dDAC-2 and dDAC-3) are similar to differences between previously published measurements [18,19,27], and between the three single-crystal X-ray diffraction experiments reported in Loubeyre *et al*. [27]. The scatter that we see in our data within one run is significantly smaller than in any of the experiments previously reported [18,19,27].

Our data generally agree with equations-of-state based on both experimental data [43] and computational results [42], even though some small but systematic deviations in P-trends exist in the P-range 50-100 GPa (Fig. 4c). This range coincides with the formation of the disordered ice state(s), likely triggered by nuclear quantum effects occurring in the range 50 $\lesssim P \lesssim$ 70 GPa [13,14]. French & Redmer [42] computed an analytical thermodynamic potential from ab-initio calculations based on classical proton trajectories; although their calculations were supplemented with a quantum correction, they did not include tunnelling effects, which affect the proton motion and can explain the deviation from our results. The equation of state by Klotz *et al.* [43] is based on the extrapolation of neutron diffraction data measured up to 14 GPa, which is a too low P for observing significant proton tunnelling effects as indicated by the NMR results [29].

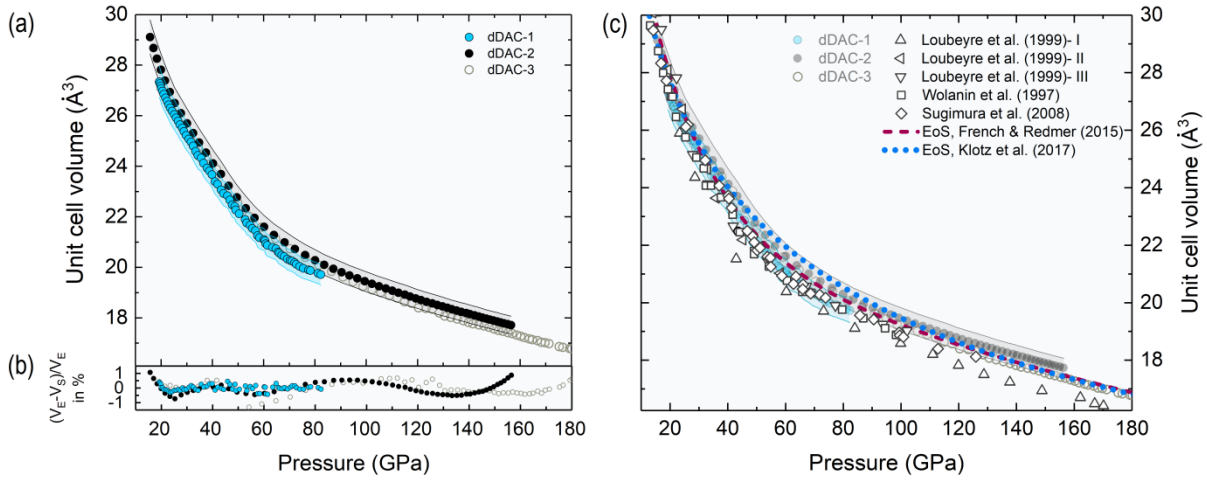

Figure 4. (a) Volume-pressure points for H_2O ice as derived from the reduced datasets of the dDAC-1 (blue solid circles), dDAC-2 (black solid circles) and dDAC-3 data (grey open circles). Error bands using the resolution limit (0.05° in 2θ) of the fitting routine are shown for dDAC-1 and dDAC-2 (shaded regions). (b) Difference between the data points and the spline with smoothing factors of 9.0 (dDAC-1), 1.0 (dDAC-2) and 18.0 (dDAC-3) is <1% over the complete compression range for all experiments. (c) Previous XRD measurements in static DAC experiments by Wolanin *et al.* [19] (powder, squares), Sugimura *et al.* [18] (powder, diamonds) and Loubeyre *et al.* [27] (three single-crystal datasets, three differently pointing triangles) are plotted in comparison to our data. The dashed (maroon) and dotted (blue) curves represent the equations-of-state by French & Redmer [42] and Klotz *et al.* [43], respectively, the latter extrapolated significantly beyond the *P*-range of the experiments (14 GPa).

3.2. Bulk modulus of H_2O ice at high pressures

Bulk moduli computed from our splined data (for clarity we only show K_T-P from dDAC-2 in Fig. 5, with the results for dDAC-1 and dDAC-3 in Fig. S2 of the Supplemental Material) agree well with recent Brillouin spectroscopy measurements at $P \lesssim 35$ GPa [44,45]. At higher P, three major changes in the slope of K_T-P are captured by our experiments (Fig. 5):

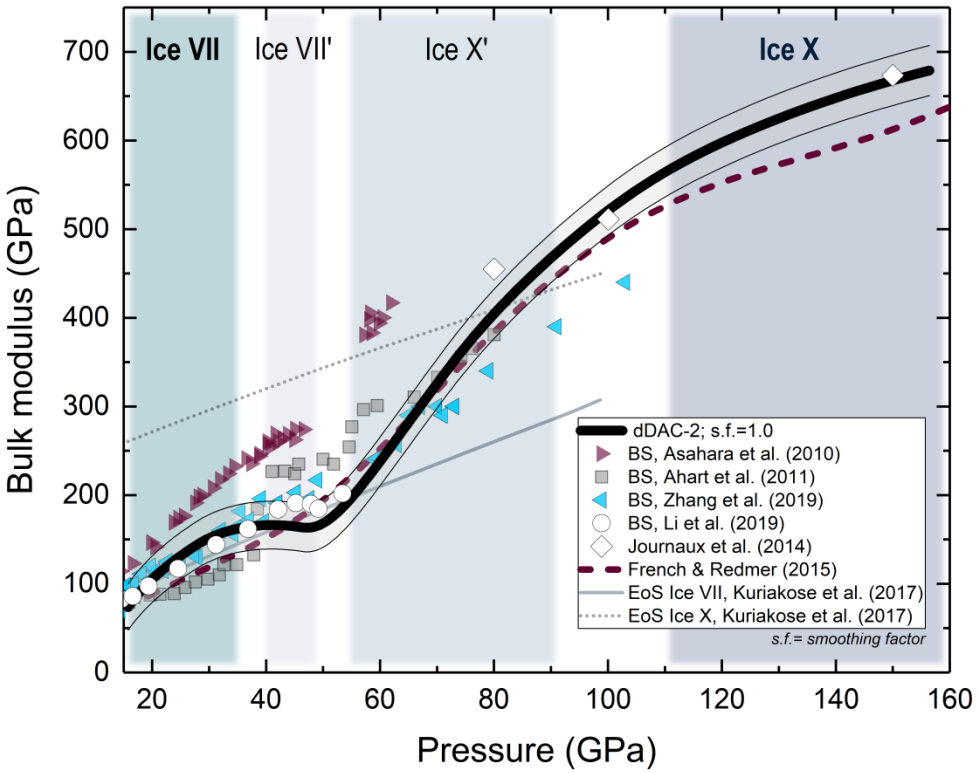

234

235 **Figure 5.** Bulk modulus of H_2O ice as a function of pressure calculated from the smoothed
236 spline interpolation of the $V(P)$ data from dDAC-2 in comparison to previous studies (for
237 results from dDAC-1 and dDAC-3, see Fig. S2 in Supplemental Material). Right-pointing
238 triangles, solid squares, left-pointing triangles and solid circles represent Brillouin inelastic
239 scattering (BS) data [44–47]. The solid and dotted thin grey lines show equations-of-state for
240 ice VII and ice X, respectively [48]. Diamonds represent computational predictions of the
241 bulk modulus of ice X [49]. The dashed maroon line refers to computational results [42].
242 Background colours guide the eyes to the approximate P-ranges for the stability of ice VII, ice
243 VII', ice X' and ice X based on the P-ranges where a quasi-linear P-dependence of K_T is
244 observed in our work.

245 (i) A softening starting at P=35-40 GPa indicates a transition towards a more compressible
246 state (Fig. 5), supporting previous findings [18]. We associate this change with the
247 formation of disordered ice VII'. While Brillouin spectroscopy measurements disagree
248 with one another in terms of absolute values for K_T, they show [45,46] – or at least

hint [44] at – a P-range of high compressibility (40-50 GPa), supporting our observation of highly compressible ice VII'. A possible reason for the disagreement between the various Brillouin spectroscopy studies at all P is the marked elastic anisotropy of ice VII and, as a consequence, the possibility that velocities along certain directions were favored by crystallographic preferred orientation and/or selective elasto-optic coupling between the probing laser and specific phonon propagation direction [50]. In the P-range where we observe the softening, signal overlap with the diamond-anvils further complicates a reliable determination of the bulk modulus by Brillouin spectroscopy [44].

(ii) A steep increase in K_T starting at P=50-55 GPa marks the formation of a less compressible phase, in agreement with the onset of hydrogen symmetrization predicted by computations at P≈50 GPa [13], and may also be associated with anomalies in the infrared spectra of H_2O ice reported for P=55-62 GPa [23,51,52]. We attribute this feature to the formation of ice X' [18].

(iii) A distinct change in P-dependence of K_T at P=90-110 GPa, which is in excellent agreement with computational predictions [42,49], but has not been documented by previous experiments on the elastic properties of ice VII [18,24,26–28]. We attribute this change to the formation of static ice X.

These changes in the P-behavior of K_T are also visible in the dDAC-1 and dDAC-3 data at comparable onset P (Fig. S2 in the Supplemental Material).

The observed P-evolution of K_T across the ice VII – ice X transition in our experiments can be correlated with the variations in proton mobility observed by Meier *et al.* [29] for the O-H···O bond, and be rationalized by the predicted evolution of the energy barrier of a double-well potential [17,53]. Meier *et al.* [29] documented a significant increase in tunelling probability for P=20-50 GPa, i.e., in the P-range where the formation of ice VII' is expected. Our observation of a softening of K_T for ice VII observed for P=35-40 GPa may be explained by a

decrease in the "proton pressure" caused by higher proton mobility [18,53]. The steep increase in K_T that we observe for P>50 GPa (Fig. 5) may reflect the proton centering process, and the formation of ice X'. Full proton localization may cause the change of the P-derivative in our K_T -data for P=90-110 GPa.

4. CONCLUSIONS

We have collected quasi-continuous X-ray diffraction data across the ice VII – ice X transition and up to P=180 GPa in three dynamically driven diamond-anvil-cell experiments. We derive the bulk modulus of H_2O ice directly from our $V(P)$ data. We find three main changes in the pressure-dependence at 35-40, 50-55 and 90-110 GPa and associate them with the formation of ice VII', ice X' and ice X, respectively. These transitions are not sharp; certainly not of first order (no volume collapse), unlikely of second order (no discontinuous changes in bulk modulus). This association suggests that the compressive behavior of H_2O at high pressure is sensitive to proton ordering. Our results further confirm computational predictions that the bulk modulus of ice X is distinctly higher than that of ice VII.

Acknowledgements

This research was supported through the German Science Foundation (Deutsche Forschungsgemeinschaft, DFG) in Research Unit FOR 2440 (grants MA4534/5-1 and STE1105/13-1). We acknowledge DESY (Hamburg, Germany), a member of the Helmholtz Association HG, for providing the experimental facility PETRA III and beamline P02.2. We acknowledge B. Winkler and the BMBF project 05K13RF1 for the purchase of the laser cutting machine for preparing gaskets. We thank Martin French for sharing water high-pressure results, and Tiziana Boffa Balaran, Niccolò Satta and Thomas Meier for helpful discussions.

References

[1] J.J. Lissauer *et al.*, Nature **470**, 53 (2011).
[2] R. Redmer, T. R. Mattsson, N. Nettelmann, and M. French, Icarus **211**, 798 (2011).
[3] R. Jaumann, R. N. Clark, F. Nimmo, A. R. Hendrix, B. J. Buratti, T. Denk, J. M. Moore, P. M. Schenk, S. J. Ostro, and R. Srama, in *Saturn from Cassini-Huygens*, edited by M. K. Dougherty, L. W. Esposito, and S. M. Krimigis (Springer Netherlands, Dordrecht, 2009), pp. 637–681.

[4] S.A. Kattenhorn and L.M. Prockter, Nat. Geosci. **7**, 762 (2014).
[5] B. Journaux, I. Daniel, S. Petitgirard, H. Cardon, J.-P. Perrillat, R. Caracas, and M. Mezouar, Earth Planet. Sc. Lett. **463**, 36 (2017).
[6] L. Noack, D. Höning, A. Rivoldini, C. Heistracher, N. Zimov, B. Journaux, H. Lammer, T. Van Hoolst, and J. H. Bredehöft, Icarus **277**, 215 (2016).
[7] C. Sotin, O. Grasset, and A. Mocquet, Icarus **191**, 337 (2007).
[8] A.D. Fortes and M. Choukroun, Space. Sci. Rev. **153**, 185 (2010).
[9] J.-F. Lin, V. V. Struzhkin, S. D. Jacobsen, M. Y. Hu, P. Chow, J. Kung, H. Liu, H.-k. Mao and R. J. Hemley, Geophys. Res. Lett. **32**, L11306 (2005).
[10] B. Schwager and R. Boehler, High Pressure Res. **28**, 431 (2008).
[11] O. Tschauner, S. Huang, E. Greenberg, V. B. Prakapenka, C. Ma, G. R. Rossman, A. H. Shen, D. Zhang, M. Newville, A. Lanzirotti, and K. Tait, Science **359**, 1136 (2018).
[12] J. D. Bernal and R. H. Fowler, J. Chem. Phys. **1**, 515 (1933).
[13] W.B. Holzapfel, J. Chem. Phys. **56**, 712 (1972).
[14] M. Benoit, D. Marx, and M. Parrinello, Nature **392**, 258 (1998).
[15] M. Benoit, A. H. Romero, and D. Marx, Phys. Rev. Lett. **89**, 145501 (2002).
[16] M. Benoit and D. Marx, ChemPhysChem **6**, 1738 (2005).
[17] L. Lin, J.A. Morrone, and R. Car, J. Stat. Phys. **145**, 365 (2011).
[18] E. Sugimura, T. Iitaka, K. Hirose, K. Kawamura, N. Sata, and Y. Ohishi, Phys. Rev. B **77**, 214103 (2008).
[19] E. Wolanin, Ph. Pruzan, J. C. Chervin, B. Canny, M. Gauthier, D. Häusermann, and M. Hanfland, Phys. Rev. B **56**, 5781 (1997).
[20] M. Guthrie, R. Boehler, J. J. Molaison, B. Haberl, A. M. dos Santos, and C. Tulk, Phys. Rev. B **99**, 184112 (2019).
[21] A.F. Goncharov, N. Goldman, L.E. Fried, J.C. Crowhurst, I. Feng W. Kuo, C.J. Mundy, and J.M. Zaug, Phys. Rev. Lett. **94**, 125508 (2005).
[22] K. Aoki, H. Yamawaki, M. Sakashita, and H. Fujihisa, Phys. Rev. B **54**, 15673 (1996).
[23] A. F. Goncharov, V. V. Struzhkin, M. S. Somayazulu, R. J. Hemley, and H. K. Mao, Science **273**, 218 (1996).
[24] M. Song, H. Yamawaki, H. Fujihisa, M. Sakashita, and K. Aoki, Phys. Rev. B **60**, 12644 (1999).
[25] M. Song, H. Yamawaki, H. Fujihisa, M. Sakashita, and K. Aoki, Phys. Rev. B **68**, 014106 (2003).
[26] C.-S. Zha, R.J. Hemley, S.A. Gramsch, H. Mao, and W.A. Bassett, J. Chem. Phys. **126**, 074506 (2007).
[27] P. Loubeyre, R. LeToullec, E. Wolanin, M. Hanfland, and D. Hausermann, Nature **397**, 503 (1999).
[28] C.-S. Zha, J.S. Tse, and W.A. Bassett, J. Chem. Phys. **145**, 124315 (2016).
[29] T. Meier, S. Petitgirard, S. Khandarkhaeva, and L. Dubrovinsky, Nat. Commun. **9**, 2766 (2018).
[30] W.J. Evans, C.-S. Yoo, G.W. Lee, H. Cynn, M.J. Lipp, and K. Visbeck, Rev. Sci. Instrum. **78**, 073904 (2007).
[31] Zs. Jenei *et al.*, Rev. Sci. Instrum. **90**, 065114 (2019).
[32] A.S.J. Méndez, H. Marquardt, R.J. Husband, I. Schwark, J. Mainberger, K. Glazyrin, A. Kurnosov, C. Otzen, N. Satta, and J. Bednarcik, Rev. Sci. Instrum. **91**, https://doi.org/10.1063/5.0007557 (2020).
[33] H.-P. Liermann *et al.*, J. Synchrotron Radiat. **22**, 908 (2015).
[34] D. Pennicard *et al.*, J. Instrum. **13**, C01026 (2018).
[35] D. Pennicard, S. Lange, S. Smoljanin, H. Hirsemann, H. Graafsma, M. Epple, M. Zuvic, M.-O. Lampert, T. Fritzsch, and M. Rothermund, J. Phys. Conf. Ser. **425**, 062010 (2013).
[36] C. Prescher and V.B. Prakapenka, High Pressure Res. **35**, 223 (2015).

[37] S.P. Ong, W.D. Richards, A. Jain, G. Hautier, M. Kocher, S. Cholia, D. Gunter, V.L. Chevrier, K.A. Persson, and G. Ceder, Comput. Mater. Sci. **68**, 314 (2013).
[38] Matt Newville *et al.*, *Lmfit/Lmfit-Py 1.0.1* (Zenodo, 2020).
[39] Y. Fei, A. Ricolleau, M. Frank, K. Mibe, G. Shen, and V. Prakapenka, PNAS **104**, 9182 (2007).
[40] P. Dierckx, J. Comput. Appl. Math. **1**, 3 (1975).
[41] P. Dierckx, SIAM J. Numer. Anal. **19**, 1286 (1982).
[42] M. French and R. Redmer, Phys. Rev. B **91**, 014308 (2015).
[43] S. Klotz, K. Komatsu, H. Kagi, K. Kunc, A. Sano-Furukawa, S. Machida, and T. Hattori, Phys. Rev. B **95**, 174111 (2017).
[46] J. S. Zhang, M. Hao, Z. Ren, and B. Chen, Appl. Phys. Lett. **114**, 191903 (2019).
[45] X. Li, W. Shi, X. Liu, and Z. Mao, Amer. Miner. **104**, 1307 (2019).
[44] M. Ahart, M. Somayazulu, S.A. Gramsch, R. Boehler, H. Mao, and R.J. Hemley, J. Chem. Phys. **134**, 124517 (2011).
[47] Y. Asahara, K. Hirose, Y. Ohishi, N. Hirao, and M. Murakami, Earth Planet. Sci. Lett. **299**, 474 (2010).
[48] M. Kuriakose, S. Raetz, Q. M. Hu, S. M. Nikitin, N. Chigarev, V. Tournat, A. Bulou, A. Lomonosov, P. Djemia, V. E. Gusev, and A. Zerr, Phys. Rev. B **96**, 134122 (2017).
[49] B. Journaux, R. Caracas, P. Carrez, K. Gouriet, P. Cordier, and I. Daniel, Phys. Earth Planet. In. **236**, 10 (2014).
[50] S. Speziale, H. Marquardt, and T.S. Duffy, Rev. Mineral. Geochem. **78**, 543 (2014).
[51] A.F. Goncharov, V.V. Struzhkin, H. K. Mao, and R.J. Hemley, Phys. Rev. Lett. **83**, 1998 (1999).
[52] V.V. Struzhkin, A.F. Goncharov, R.J. Hemley, and H. K. Mao, Phys. Rev. Lett. **78**, 4446 (1997).
[53] M. Benoit and D. Marx, ChemPhysChem **6**, 1738 (2005).

Bulk modulus of H_2O across the ice VII – ice X transition measured by time-resolved X-ray diffraction in dynamic Diamond Anvil Cell experiments

Supplemental Material

A. S. J. Méndez[1, 2], F. Trybel[2], R. J. Husband[1], G. Steinle-Neumann[2], H.-P. Liermann[1] and H. Marquardt[3]

[1]Deutsches Elektronen-Synchrotron (DESY), 22607 Hamburg, Germany; [2]Bayerisches Geoinstitut, Universität Bayreuth, 95440 Bayreuth, Germany; [3]Department of Earth Sciences, University of Oxford, OX1 3AN Oxford, UK.

*Corresponding author: Alba San José Méndez (alba.mendez@desy.de)

This file contains supplemental information on the following:

(i) A comparison of P and V obtained from our X-ray diffraction peak fitting with Gaussian functions to LeBail refinement on a number of selected diffraction patterns of the dDAC-1 and dDAC-2 experiments (Table S1).

(ii) Further information on data reduction, i.e., the $V(P)$ curves for the full dataset from the dDAC-2 experiments and the calculations of the bulk modulus K_T (Figure S1).

(iii) A comparison of the bulk modulus K_T calculated from the smoothed splined results of the dDAC-1, dDAC-2 and dDAC-3 experiments (Figure S2).

Peak analysis: In our diffraction patterns, each peak is individually fitted to a Gaussian with a linear background correction. This approach appears superior to a Rietveld or Le Bail refinement (i) when it comes to peak-overlaps and (ii) automation of data processing. In order to assess the consistency of our results, we have performed a Le Bail fit on a limited number of diffraction patterns from dDAC-1 and dDAC-2 and compared the P and V obtained from both approaches in Table S1. The Gaussian and Le Bail fits are consistent with one another within the error coming from the minimal separable peak distance in our approach (2θ=0.05°) using individual Gaussian.

Table S1. Comparison for ten points (five each for dDAC-1 and dDAC-2) for P and V using Le Bail and Gaussian fitting to X-ray diffraction patterns. The errors given in the V-estimate from our Gaussian fit ($V_{Gaussian}$) reflect the minimal separable peak (2θ=0.05°). Volume uncertainties from the LeBail fit (V_{LeBail}) are below 10^{-2} Å^3.

Experiment/Frame	$V_{Gaussian}$ (Å^3)	$P_{Gaussian}$ (GPa)	V_{LeBail} (Å^3)	P_{LeBail} (GPa)
dDAC-1/450	27.2(6)	19.8	27.3	19.9
dDAC-1/700	25.9(6)	25.9	26.2	25.5
dDAC-1/950	24.4(5)	34.3	24.8	34.2
dDAC-1/1275	22.4(5)	48.7	22.5	49.0
dDAC-1/1875	20.3(4)	71.1	20.4	71.1
dDAC-2/230	27.8(6)	19.9	27.9	19.7
dDAC-2/260	26.5(6)	25.3	26.5	25.2
dDAC-2/390	21.3(4)	64.0	21.3	64.0
dDAC-2/510	19.3(4)	105.0	19.3	104.4
dDAC-2/650	18.3(4)	135.2	18.4	134.7

Data reduction: The volume changes caused by the fine pressure steps that characterize our quasi-continuous compression data are, in general, below the fitting resolution, especially for high values of K_T where the sample is highly incompressible. Under such conditions, small shifts in 2θ-space of the traced reflections cannot be resolved by the fitting program. These factors can introduce artificial jumps in the $V(P)$ data that are magnified in the derivative. In order to avoid this, we increase the P-steps by skipping patterns in the fitting. An example of such procedure is illustrated for dDAC-2 in Fig. S1a. The bulk modulus is then calculated from the reduced dataset by three-point finite differences before smoothing, and compared

with K_T obtained after applying a spline interpolation and smoothing for the reduced dataset (Fig. S1b). The main features in the P-dependence of K_T are conserved after smoothing the reduced dataset.

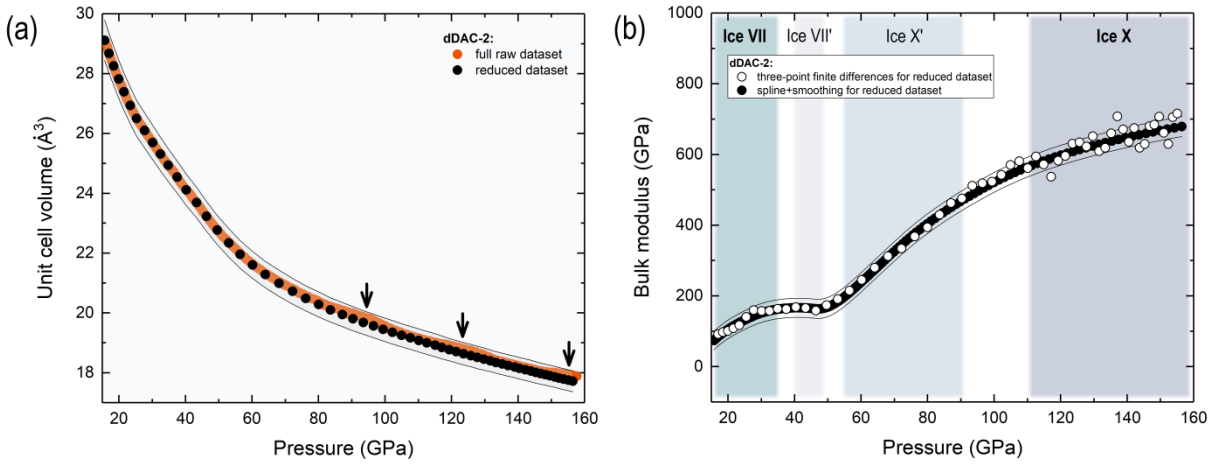

Figure S1. (a) Pressure-volume curves for dDAC-2. Orange circles correspond to the analysed full data consisting of 590 diffraction patterns, black circles represent *V(P)* data obtained after fitting every 10th pattern (reduced dataset) as described in Section 2.3. Black thin lines indicate the error in *V*. Black arrows point to small artificial jumps in the full *V(P)* data set, introduced by the fitting routine. (b) Bulk modulus as a function of pressure derived from the reduced dataset in dDAC-2, following two different procedures: (i) Computed by three-point finite differences (white circles) and (ii) derived from the procedure described in Section 2.4 using the reduced dataset (black circles).

Comparison of bulk modulus from different runs: Bulk moduli K_T derived from dDAC-1, dDAC-2 and dDAC-3 are plotted against P in Fig. S2**,** in comparison to computational results from French & Redmer [42]. Overall, the P-dependence of K_T agrees between the three experiments and with the computational results. The three main changes in P-dependence of K_T – discussed for the dDAC-2 data in the main text – are also visible in dDAC-3, despite fluctuations noticeable above 100 GPa which originate from modulations in the *V(P)* curve introduced by the fitting routine. The magnitude of these fluctuations falls within experimental uncertainty. With a maximum P=90 GPa reached in the dDAC-1 experiment, only the signature of the ice VII – ice VII' and ice VII' – ice X' is observed.

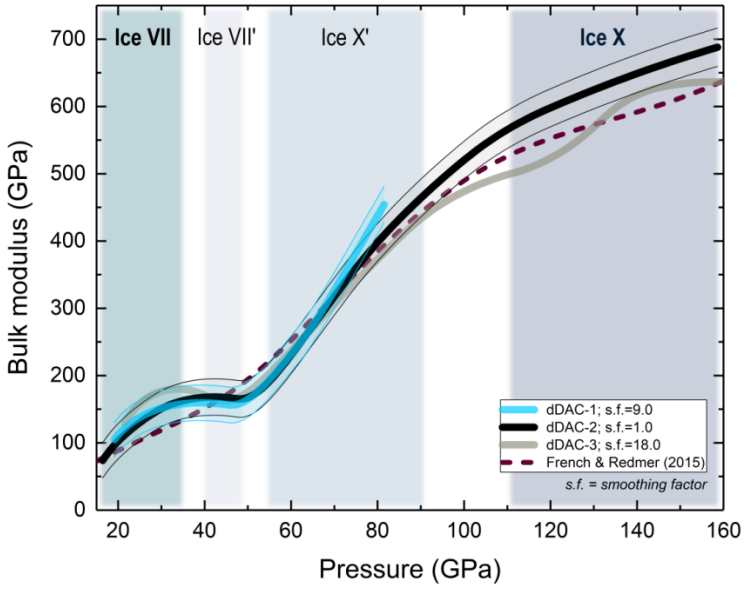

Figure S2. Bulk modulus as a function of pressure as derived from dDAC-1, dDAC2 and dDAC-3 data. The dashed maroon line shows computational results [42]. Background colors indicate approximate *P*-ranges for the stability of ice VII, ice VII', ice X' and ice X based on the *P*-ranges where a quasi-linear *P*-dependence of K_T is observed in our work.